Chapter 7

High Speed Imager Calibration

Ian Evans

7.1 Introduction

The current status of the calibration of the High Speed Imager (*HSI*) microchannel-plate based x-ray imaging detector (Evans et al., 1997) is reported. The *HSI* imager is part of the *HRMA* X-ray Detection System (*HXDS*) that was used during Phase 1 of the *AXAF* calibrations at the *MSFC* X-Ray Calibration Facility (Weisskopf and O'Dell, 1997).

Immediately prior to the beginning of Phase 1 calibrations at the *XRCF*, the *HSI* microchannel-plate assembly was replaced. Therefore, no valid pre-Phase 1 calibration data exist for the *HSI*. Calibration of the *HSI* was performed, primarily at the *SAO* X-ray Pipe Facility (*XPF*), during October and November, 1997.

At the time of writing, all the calibration data have been inspected and qualitative studies of the data have been performed. However, detailed quantitative analyses have not yet been completed. Therefore, we present here a description of the *HSI* calibration data, and a discussion of calibration features significant to scientists who are analyzing *HRMA* calibration data obtained using the *HSI*.

7.2 Calibration Data Summary

The following calibration data were obtained at the *SAO XPF*:

- Quantum efficiency measurements at several energies and for several angles of incidence,
- Electronics count rate linearity/dead-time measurements,
- Flat fields at several energies for normal incidence,
- A pinhole mask image at one energy, to measure spatial distortion.

Additionally, the x-ray transmission of the ion shield across the principal element edges was measured at the *BESSY* facility.

Detailed descriptions of the calibration data obtained, and relevant features identified in the calibration data, are presented below.

7.3 *HSI* Quantum Efficiency Measurements

The area-averaged mean quantum efficiency (*QE*) of the *HSI* was measured by exposing the *HSI* to a nominally uniform x-ray flat field generated using an Manson electron impact source. The *HSI* count rate is determined from the secondary science fast event discriminator event counter. Without changing the x-ray source, the *HSI* is removed from the beam and a *HXDS* flow proportional counter (*fpc_hb*) (Wargelin et al., 1997) is inserted into the beam at the same location. Comparison of the *HSI* count rate with the *FPC* dead-time corrected count rate provides a *QE* calibration relative to the (TBD) *fpc_hb* counter efficiency. During the measurements, a second flow proportional counter was used to monitor and correct for temporal variations of the x-ray beam intensity.

These measurements were obtained at the following 11 energies: B-Kα, C-Kα, O-Kα, Fe-Lα, Cu-Lα, Mg-Kα, Al-Kα, Mo-Lα, Sn-Lα, Ti-Kα, and Fe-Kα (Figure 7.1). Because the *HSI* has essentially no energy discrimination, the Manson source high voltage was restricted to twice the line energy for these measurements. An approximately one mean-free-path (*mfp*) thickness source filter made of either the same material, or $Z-1$, was used to further supress the high energy continuum.

For these calibrations, a target value of 40,000 counts in the *HSI* was used to provide $\sim$0.5% statistical errors.

To calibrate the variation of *QE* as a function of x-ray incident angle, data were obtained with the *HSI* rotated at several angles around the Z axis. Such rotation alters the angle between the incident x-ray photons and the microchannel-plate pore axis. The latter is nominally rotated 6° around the *HSI* Z axis from normal incidence, with the front of the pores being offset in the $+Y$ direction. In practice, ring focus images obtained during Phase 1 *HMRA* calibrations at the *XRCF* suggest that the rotation axis is offset by about $\sim$10–12′ from the Z axis, so that the front of the microchannel-plate pores is offset slightly in the $-Z$ direction in addition to the $+Y$ direction.

Data were obtained for incident angles corresponding to Z axis rotations of $-8.0°$ to $+8.0°$ in 0.5° increments ($+6.0°$ corresponds to the *nominal* pore axis angle). For Z axis rotations $|\theta| > \sim 6.0°$ the microchannel-plates were only partly illuminated because of obscuration by the *HSI* gate valve structure. For these incident angle data, the measured count rates must be corrected for the fractional microchannel-plate area illuminated by the x-ray beam. However, this has not been done in the data presented in the figures.

7.4 Count Rate Linearity

The *HSI* counting rate response is modified by the dead-time inherent in the post-processing electronics. For compact sources, local pore-saturation effects in the microchannel-plates also reduces the detected count rate.

The *HSI* post-processing electronics detects an event when the summed $(Y+Z)$ output signal from the cross-grid charge detector exceeds a programmable threshold. Once an event is detected, the position of the event must be determined, and the event is processed by veto logic that determines whether the event is "valid" or not. In configuration used at the *XRCF*, to be valid an event must be detected in both Y and Z (so that its position can be localized), and must occur sufficiently after the previous event that the analog electronics (preamplifiers, sample and hold detectors) have returned to normal operations, and the digital electronics have completed the event processing cycle.

Because the event processing time is relatively long, imaging event processing saturates at a relatively low count rate, of order 2,500 Hz. Therefore, the *HSI* incorporates a secondary science

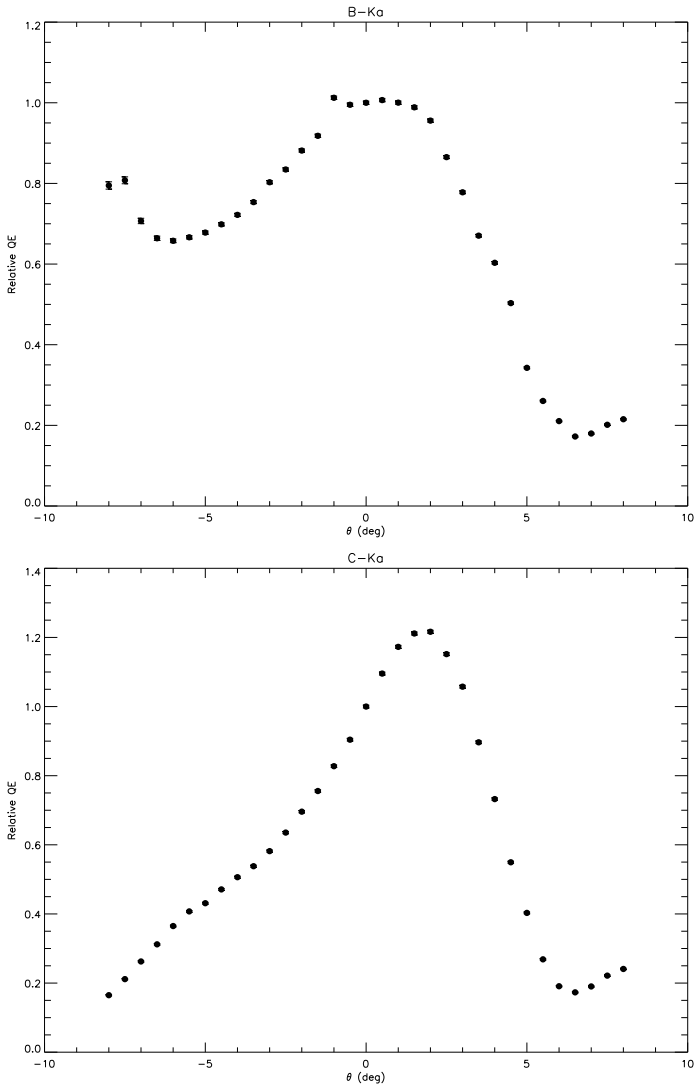

Figure 7.1: Angular dependence of relative quantum efficiency. θ is the angle to the normal of the MCP face, around the Z axis. $(\theta - 6)$ is the angle of the beam relative to the pore axis. Points marked with open circles are not corrected for known vignetting, and therefore represent a lower limit to the relative quantum efficiency. B-K and C-K.

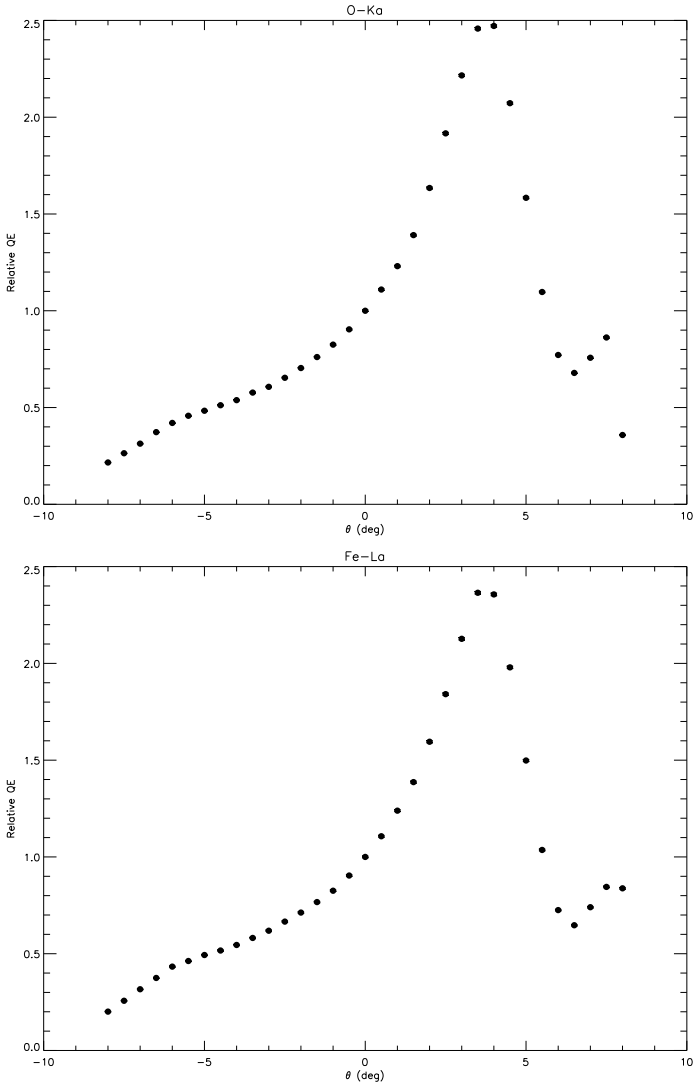

Figure 7.1: (continued) O-K and Fe-L.

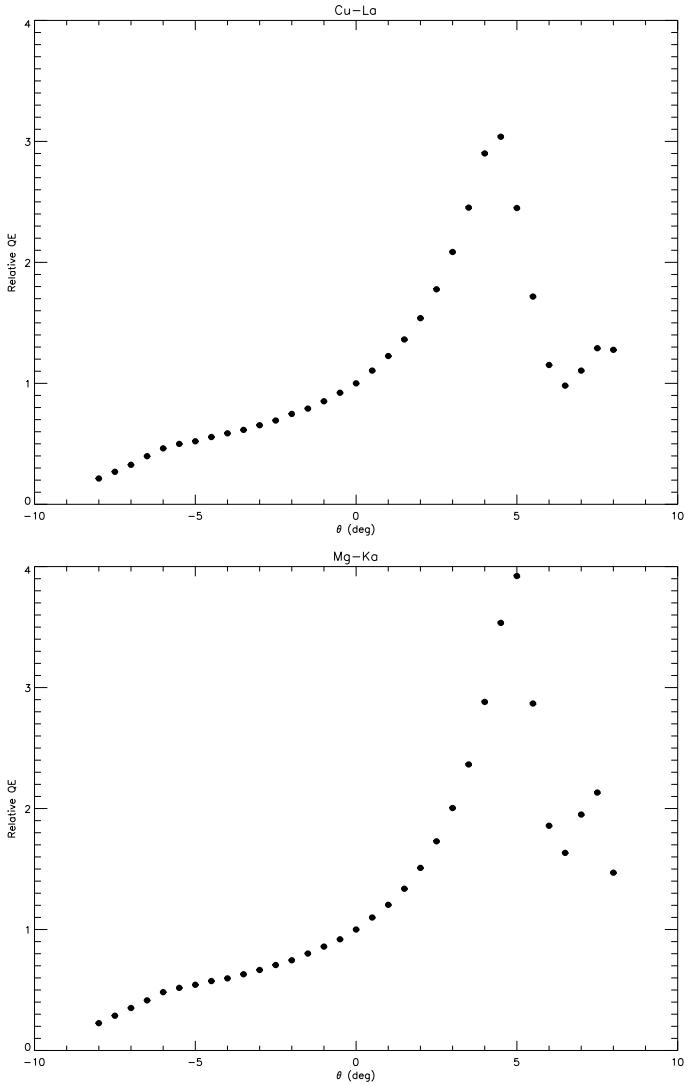

Figure 7.1: (continued) Cu-L and Mg-K.

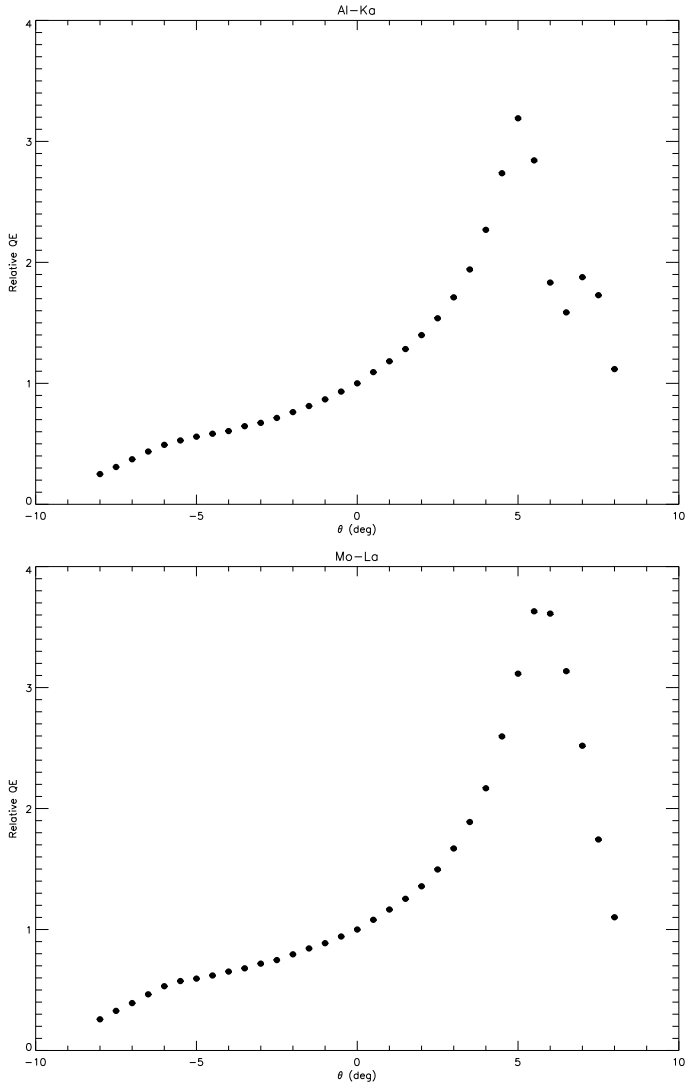

Figure 7.1: (continued) Al-K and Mo-L.

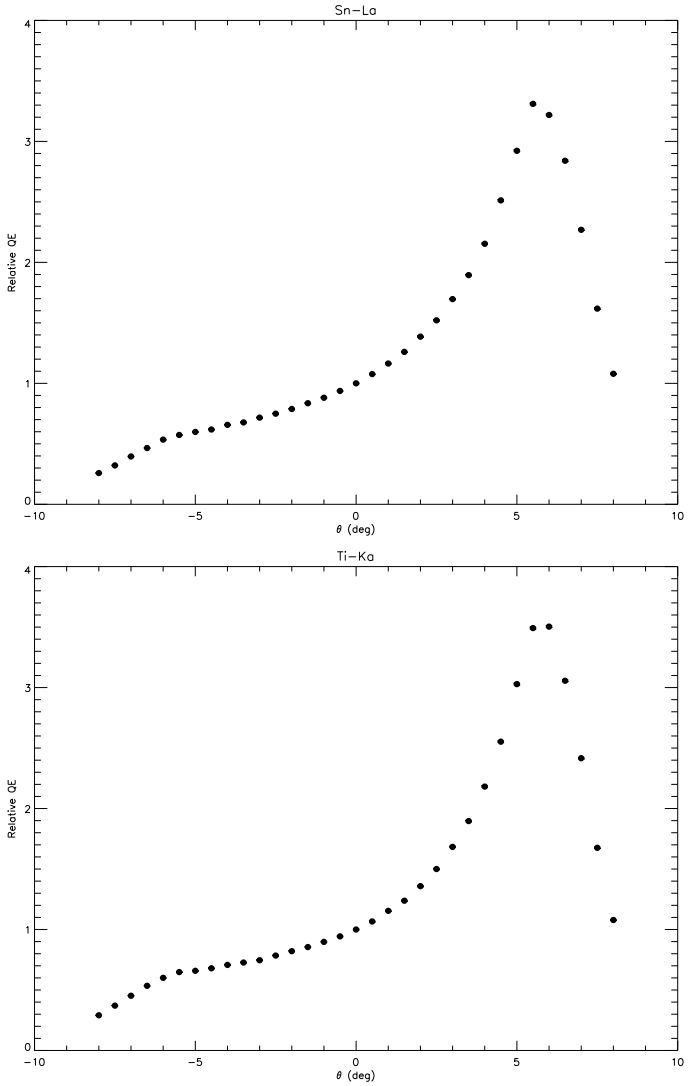

Figure 7.1: (continued) Sn-L and Ti-K.

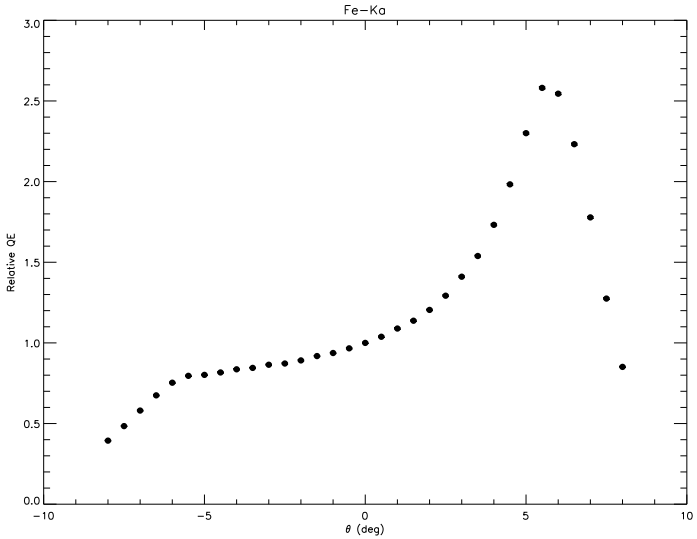

Figure 7.1: (continued) Fe-K.

fast discriminator that simply counts detected events for which the summed $Y + Z$ signal exceeds the threshold. The dead-time of this fast discriminator is a few μs, which is completely negligible for image event rates less than 2,000 Hz (the CEI spec (SAO, 1998) maximum count rate requirement). The fast discriminator event counter is recorded in the FITS file header with the keyword `FASTEVNT`. (Note that the secondary science counters do not accumulate counts for exactly the same time as the imager; therefore, when the most precise knowledge of the fast event rate is required, the fast event counter time must be derived from the number of event counter major frames recorded in the FITS file header with the keyword `NUMCTRMF`.)

The post-processing electronics count rate linearity was measured using an Al-Kα flat field and range of *HSI* event rates from $\sim$15 Hz to $\sim$2,200 Hz. The observed *HSI* count rate were referenced to the rate observed in a monitor flow proportional counter. For the figures presented here, the variation of the monitor *FPC* dead-time with rate is assumed to be accurately represented by the internal Gedke-Hale circuitry over the range of count rates considered here. Error due to counting statistics is $\sim$0.5%.

The data demonstrate that the *HSI* fast event discriminator has no significant dead-time correction for event rates up to at least 2,200 Hz (Figure 7.2). However, the image event rate, together with the total and valid event rates stored in secondary science counters, have significant dead-time corrections for count rates in excess of a few hundred Hz (Figure 7.3; Table 7.1).

Pore saturation effects cannot be quantified using the present calibration data since a compact ($\lesssim$ 20 μm diameter), high intensity x-ray source was not available. Measurements obtained at the *XRCF* using the *Technology Mirror Assembly* (*TMA*) suggest that pore saturation effects are insignificant for integrated *TMA* point response function profile count rates < 85 Hz, and are a few percent at $\sim$100 Hz. These measurements were made with the *HSI* using a set of microchannel-plates of identical design to those used during the Phase 1 *HRMA* calibrations. The response of

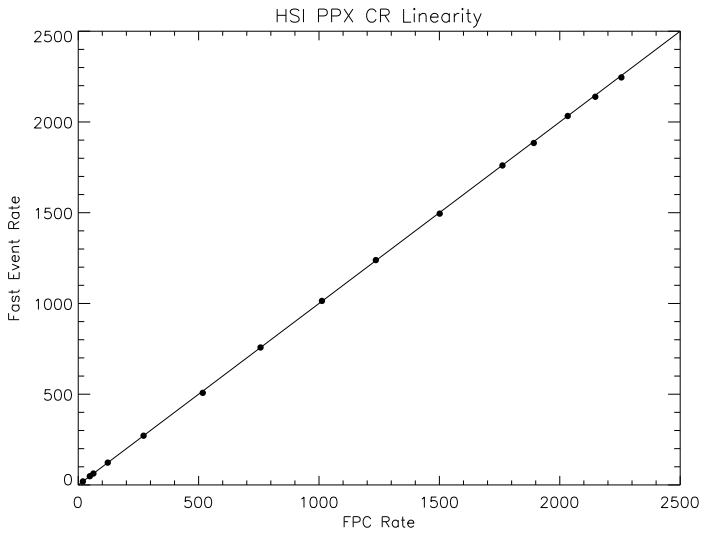

Figure 7.2: HSI post-processing electronics fast discriminator count rate linearity

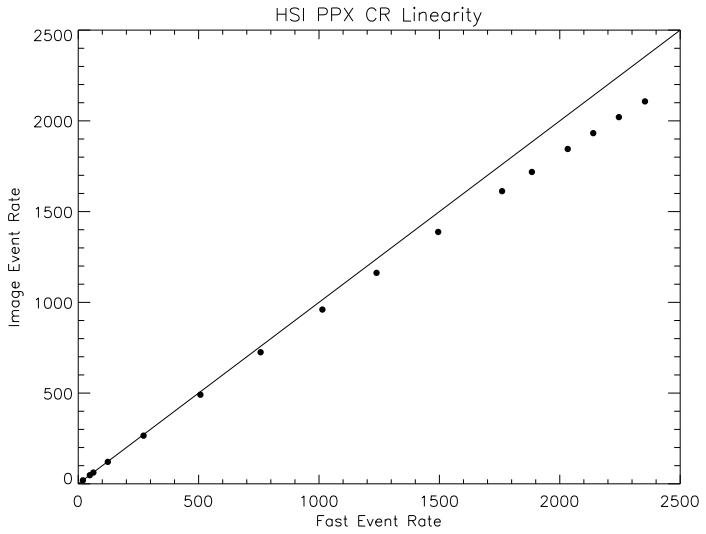

Figure 7.3: HSI post-processing electronics image count rate linearity

Fast Event Rate	Dead-Time
500 Hz	2.9%
1000 Hz	4.7%
1500 Hz	7.0%
2000 Hz	9.1%

Table 7.1: Image event rate dead-time percentages

the *HSI* in the current configuration is expected to be similar.

7.5 Flat Fields

HSI flat fields were obtained at normal incidence using an experimental setup similar to that used for the *QE* measurements. These flat fields were obtained at the following 9 line energies: C-Kα, Fe-Lα, Cu-Lα, Mg-Kα, Al-Kα, Mo-Lα, Sn-Lα, Ti-Kα, and Fe-Kα. In order to maintain an acceptable count rate, the Manson source high voltage generally was set between 3 and 4 times the line energy. These settings enhanced the high energy continuum more than is desirable, but with the high voltage limited to twice the line energy the exposure times would have been much longer than practicable.

The goal of each flat field was to obtain 4×10^7 total counts, which yields $\sim$5% statistics in a $1'' \times 1''$ area for uniform illumination.

The large scale uniformity of the x-ray beam was investigated using a *FPC* with a 2 mm diameter aperture mounted on a two axis translation stage to map the area of the beam that illuminated the *HSI*. This mapping was performed using a 69 point *listscan* (SAO, 1997) to step across the illuminated area in a raster scan with a 2 mm step size (Figure 7.4). At each point in the scan, $\sim 40,000$ counts were obtained. Thus, the statistical accuracy of the flat fields is limited on scales larger than $\sim 500\mu$m by the accuracy of the beam map. This is considered acceptable, since those features studied during Phase 1 *HRMA* calibrations that require the highest flat field accuracy have smaller scales.

Although beam uniformity measurements indicate that the *XPF* beam is very uniform within a $\sim$18 mm diameter area for most energies, this is not always true (Figure 7.5). In some cases (e.g., Sn-Lα) this non-uniformity can be traced to physical defects on the source target, while in others there is not any identifiable reason for the beam to be non-uniform. Regardless of the reason for the beam non-uniformity, an appropriate correction to the flat field data must be applied during the final calibrations.

The cosmetics of the *HSI* flat field were investigated by summing all of the flat fields obtained at individual energies to form a total summed or "super" flat field. The super flat field has approximately 3.6×10^8 overall counts, corresponding to a mean of ~ 67 counts per pixel over the illuminated area (Figure 7.6).

Immediately obvious from the super flat field is an approximately circular region of decreased sensitivity in the center of the detector (Figure 7.7). The sensitivity within a circle $\sim 150\,\mu$m diameter in the center of the detector is degraded to $\sim$75% of the surrounding uniform flat field level, and is surrounded by a annulus $\sim 250\,\mu$m wide where the sensitivity ramps up to the normal value (Figure 7.8). This is the region of the detector that was exposed to the greatest number of counts at the *XRCF*, so presumably the low sensitivity in this area is due to gain degradation caused by charge depletion in the pores of the microchannel-plates. If this is the case, it should

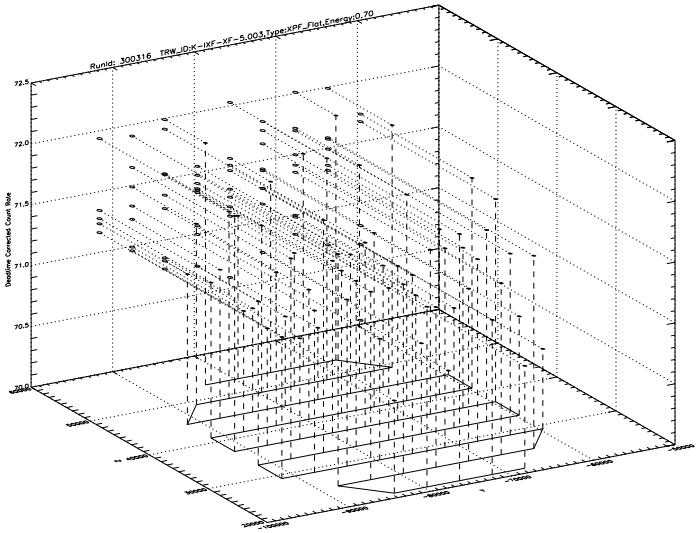

Figure 7.4: Sample flat field *FPC* scan pattern

be possible to develop a statistical correction to the observed count rate by interpolating from the total *HSI* dose maps maintained by the *AXAF Science Center* calibration group.

A few other mm scale regions of slightly degraded or enhanced sensitivity are visible in the super flat field. However, these regions are not located in areas of the detector that were used at the *XRCF* during Phase 1 calibrations (e.g., Figure 7.9).

There are several small scale cosmetic defects with much reduced sensitivity visible in the super flat field image. One of these is located ~ 1 mm from the center of the *HSI* field in the $-Y, +Z$ direction (Figure 7.10). Some small defects *may* be associated with foreign material that has settled on the ion shield, as there is evidence in some cases for correlations between defect positions and visible dust particles on the shield.

Also evident from the super flat field is variability of the width of an individual gap as a function of position along the gap (Figure 7.11). Current degapping algorithms allow for differences between the widths of individual gaps, but, because they apply on a tap by tap basis, cannot correctly degap images with gaps whose width varies along the gap. Prior flat field data had insufficient counting statistics to identify this problem. An extension of the current degapping technique that works on a tile by tile basis (rather than tap by tap) in each axis should provide adequate degapping.

Forming Y and Z projections of the super flat field reveals additional image features. The Z projection demonstrates an apparent medium spatial scale sensitivity variation in which a band in the center of each tile appears to be more sensitive than the regions of the tiles near the gaps, with a maximum peak-to-peak variation in apparent sensitivity is $\sim 9\%$ (Figures 7.12and7.13). Similar structure is visible in Y, but at much reduced amplitude. However, it is not clear whether this structure is actually caused by a spatial sensitity variation, or whether it is due to significant non-linearity of the spatial scale. Unfortunately, the available spatial distortion calibration data do not have a sufficiently fine grid to identify distortions on a scale that is significantly smaller than

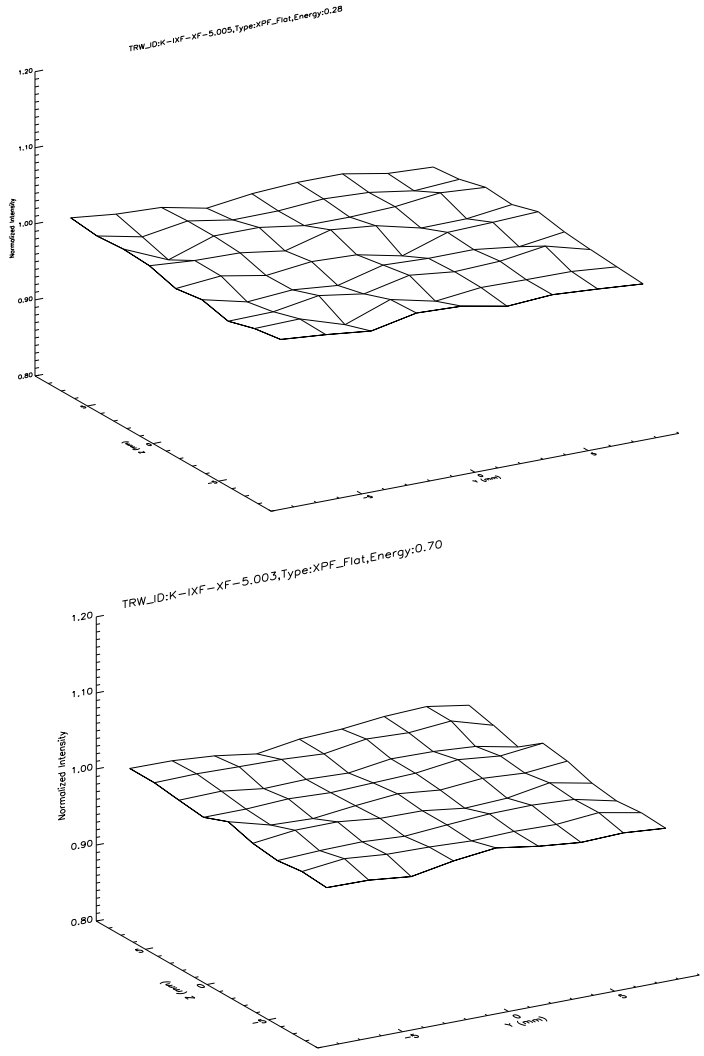

Figure 7.5: *FPC* flat field profile scans. C-K and Fe-L.

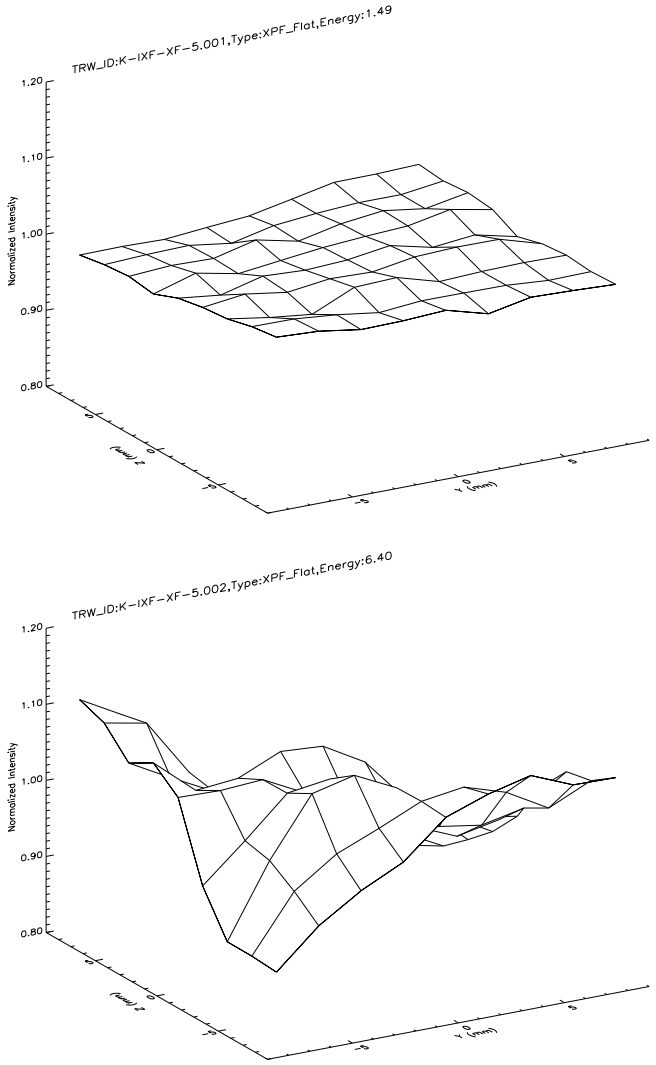

Figure 7.5: (continued) Al-K and Fe-K.

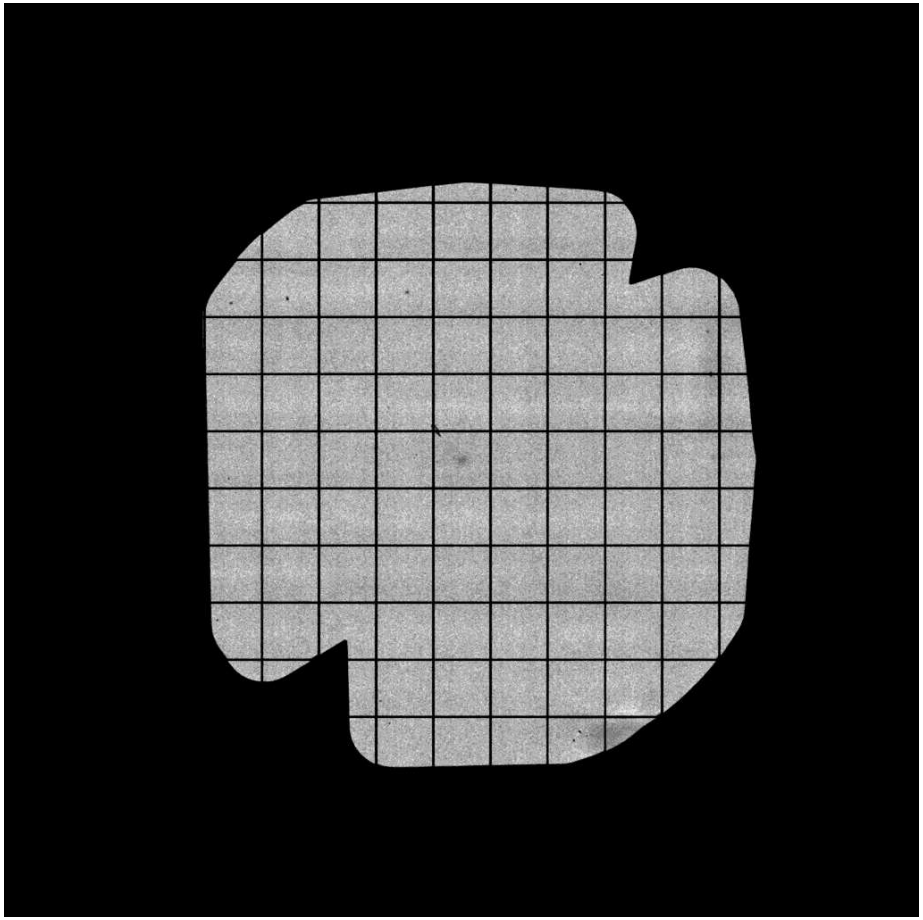

Figure 7.6: *HSI* super flat field (Y is positive to the right, Z is positive towards the top of the page). The *HSI* scale is $\sim$1.645 mm per tap.

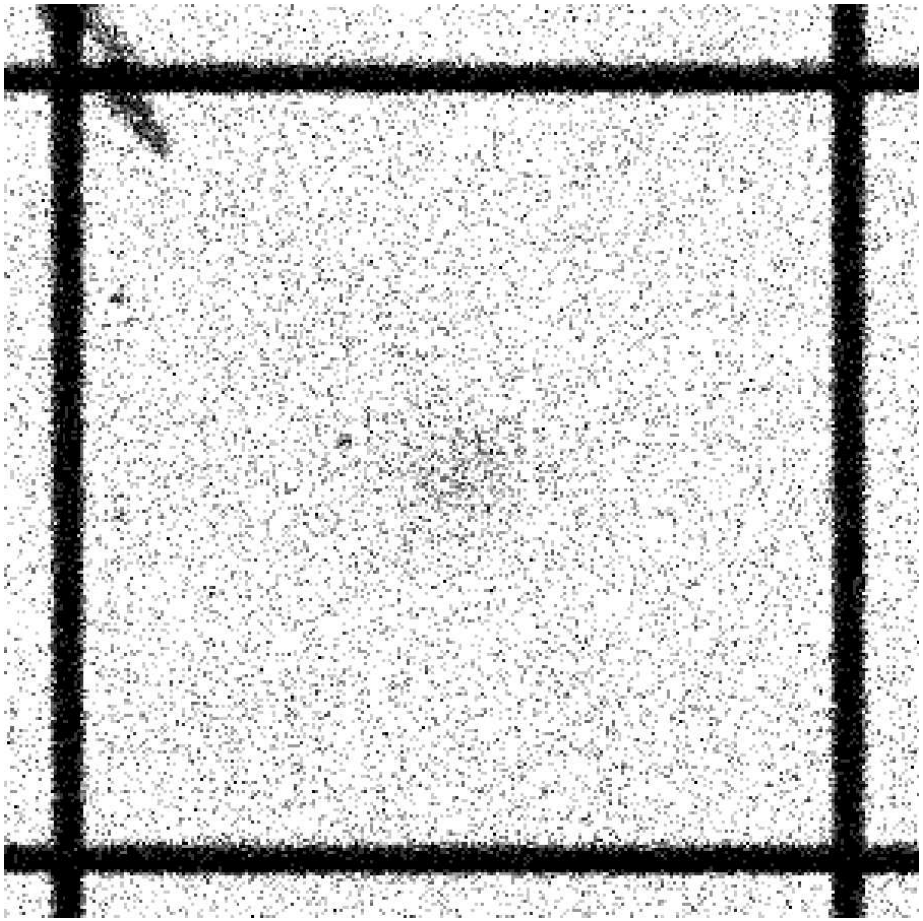

Figure 7.7: Central *HSI* tile, showing region of degraded sensitivity

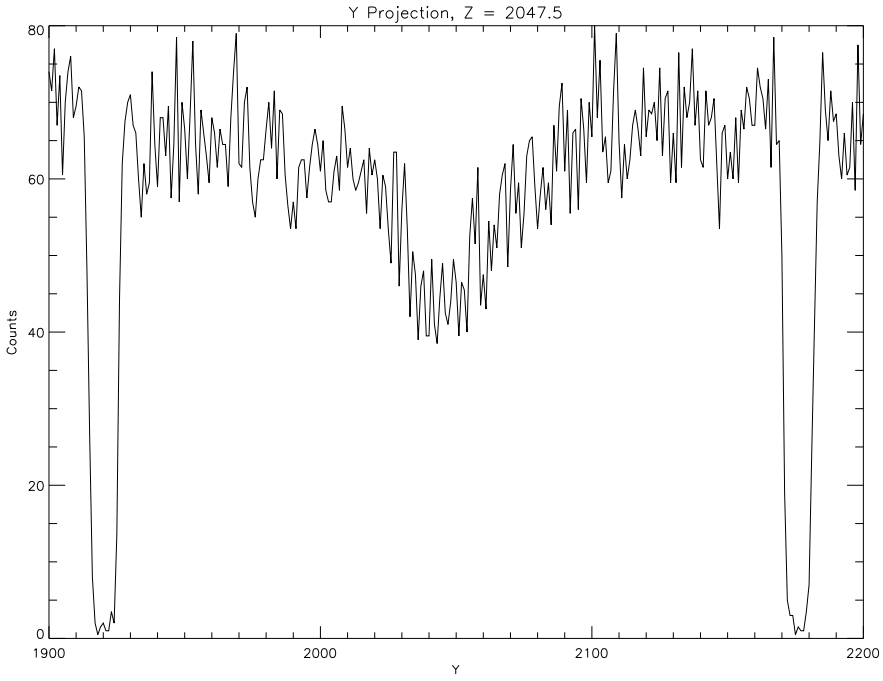

Figure 7.8: Horizontal cut across region shown in Figure 7.7. The ordinate is Y pixel number. One pixel is $\sim$6.428μm wide.

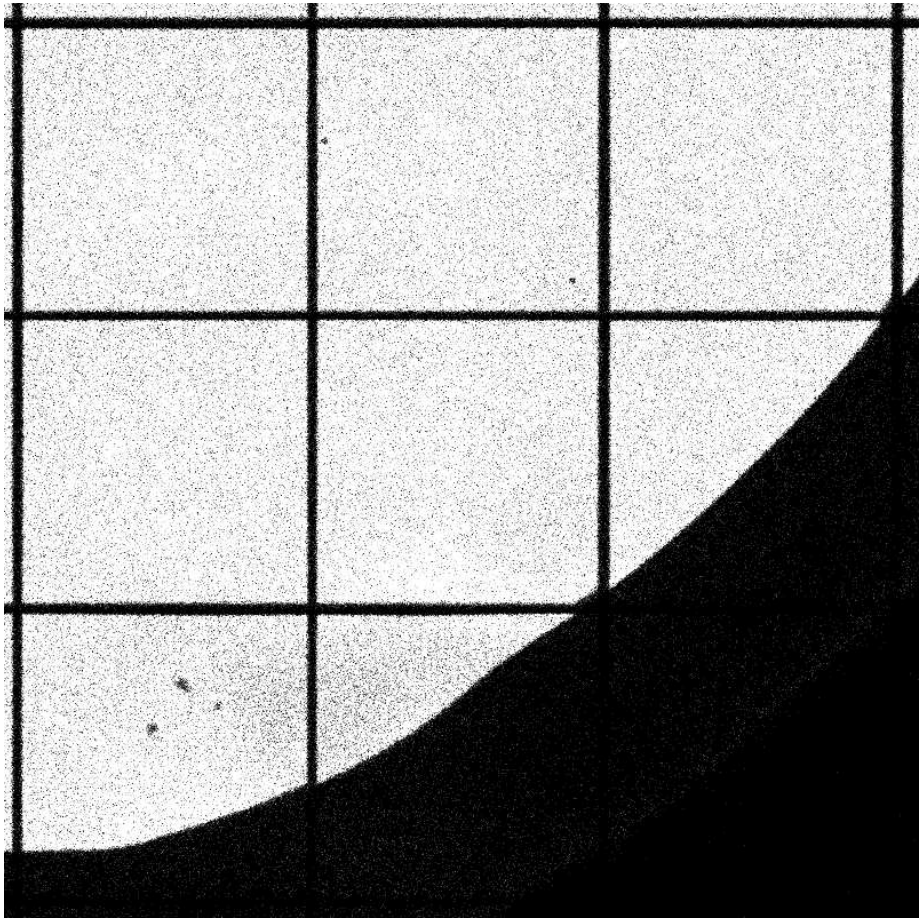

Figure 7.9: Low sensitivity region of *HSI* $(+Y, -Z)$

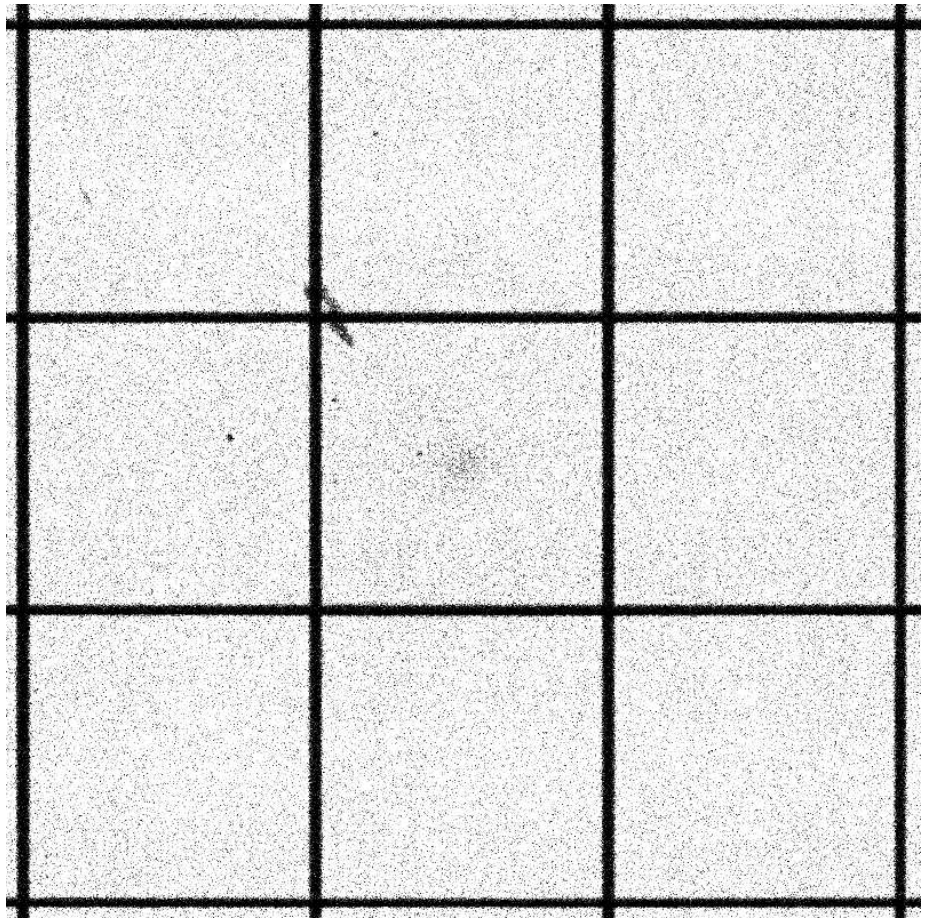

Figure 7.10: Central 3×3 tile region of *HSI* flat field

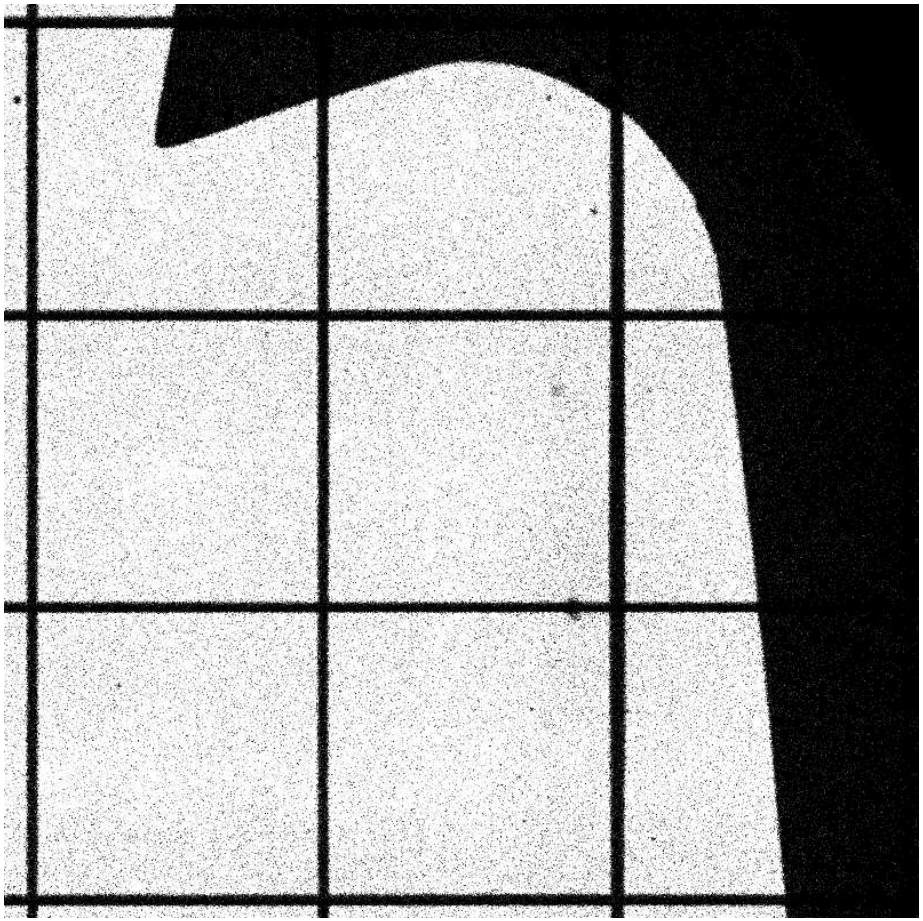

Figure 7.11: $+Y, +Z$ region of *HSI* flat field, showing variable gap width

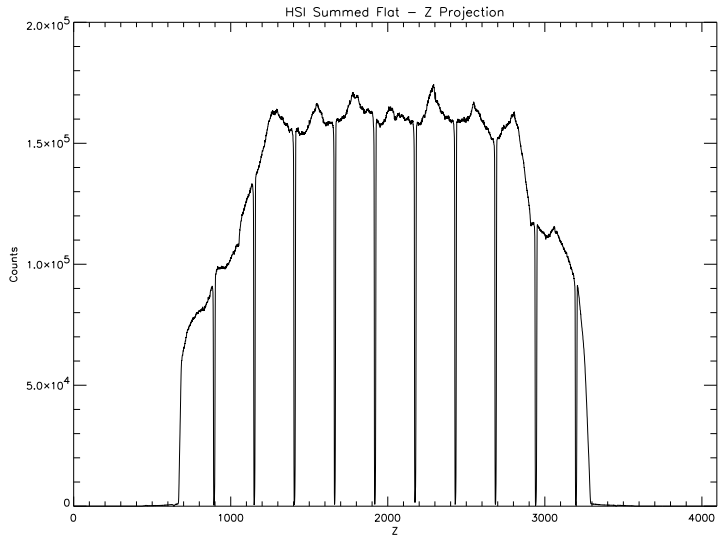

Figure 7.12: *HSI* super flat Z projection. Ordinate is Z pixel number.

one tile in size. Alternative methods of resolving this question need to be persued.

In the Y projection the dominant feature is an approximately sinusoidal apparent sensitivity variation with a maximum peak-to-peak amplitude of $\sim 5\%$ and 8 periods per tile (Figures 7.14and7.15). The peaks of the sinusoid appear to correspond to the positions of the individual cross-grid charge detector wires. These features do not appear to be evident in the Z projection. Once again, it is not clear whether spatial sensitivity variation or spatial scale distortion is responsible for these features.

7.6 Spatial Distortion

The large scale spatial distortion of the *HSI* was measured by replacing the permanent mask/ion shield assembly with a pinhole mask mounted in proximity focus to the front microchannel-plate and exposing the detector to Al-Kα x-rays. The pinhole mask consists of a rectangular grid of 50 μm diameter pinholes on 500 μm spacing. At the time of writing, the exact physical locations of the pinhole positions has not been determined through metrology. However, the manufacturer's specification states that the deviation between the actual and nominal hole positions do not exceed 2 μm. Approximately 1600 pinholes are imaged onto the *HSI* active area, and the spatial distortion corrections will be determined by mapping the centroids of pinhole images to physical pinhole locations.

Obviously, the derived spatial distortion map will be dependent on the degapping used. Because a revised degapping algorithm has not yet been tested, a spatial distortion map for the current *HSI* configuration has not yet been constructed. However, a spatial distortion map exists for a previous *HSI* configuration using similar microchannel-plates to those employed during Phase 1

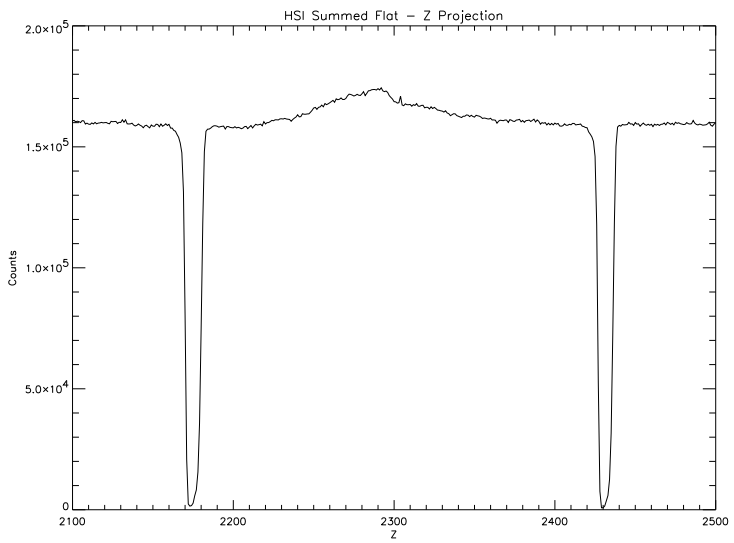

Figure 7.13: *HSI* super flat Z projection (detail). Ordinate is Z pixel number.

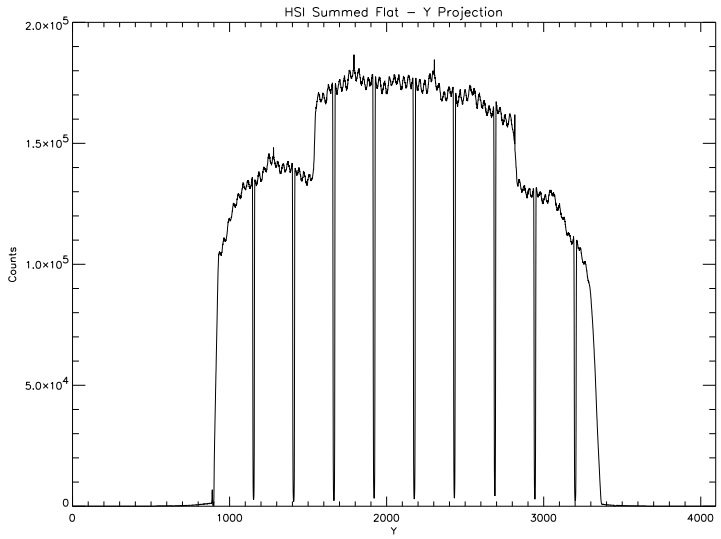

Figure 7.14: *HSI* super flat Y projection. Ordinate is Y pixel number.

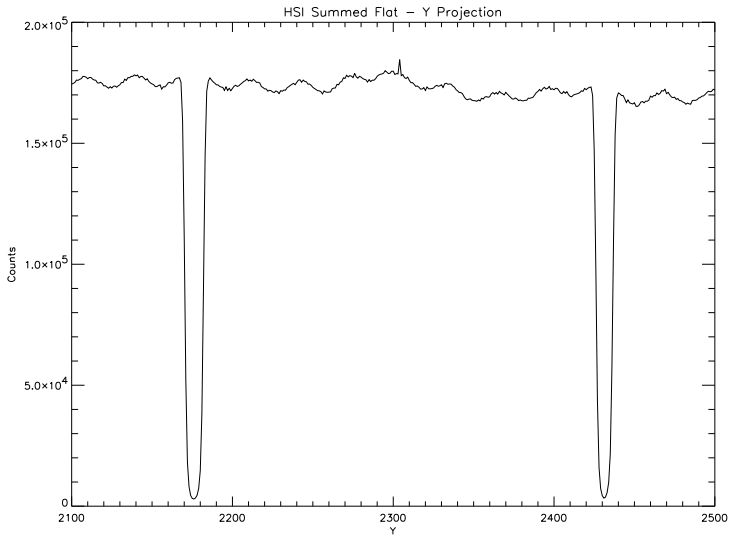

Figure 7.15: *HSI* super flat Y projection (detail). Ordinate is Y pixel number.

calibrations at the *XRCF*. That spatial distortion map revealed that measured random spatial distortions of order $10\,\mu$m were typical over most of the detector area, with some localized areas of the detector showing larger and organized distortion patterns. There was no clear evidence for any correlation between measured distortion vectors and position within tiles, *suggesting* that the apparent sensitivity variations observed in the super flat field projections are not due to spatial scale nonlinearities. If we reasonably assume that most of the spatial distortions arise due to imperfections in the construction of the cross-grid charge detector, then we would expect that the spatial distortions inherent in the current *HSI* configuration should be similar in nature to those measured for the earlier configuration.

7.7 Ion Shield Transmission

The x-ray transmission of the *HSI* ion shield used during Phase 1 *HRMA* calibration at the *XRCF* (serial number 011) was measured at the *BESSY* facility using the *SX700* monochromator beamline. The x-ray transmission was measured at three positions near the center of the ion shield at energies just above and below C, O, and Al absorption edges. The ion shield consists of a substrate of $\sim$1000 Å Lexan (H, C, and O) coated with $\sim$250 Å thickness Al.